PRISM: A Divide-and-Conquer Low-Rank and Sparse Decomposition Model for Dynamic MRI

Hao Gao*, Yuting Lin, Chang Beom Ahn, and Orhan Nalcioglu, *Fellow*, *IEEE*

***Abstract*—Image frames from dynamic MRI can be abstracted as the superposition of the background component, which is temporally coherent, and the motion component, which is spatially sparse, up to the proper basis. Inspired by their distinct characterizations, we introduce the divide-and-conquer spatiotemporal matrix decomposition approach, namely Prior Rank, Intensity and Sparsity Model (PRISM). Here the temporal coherence of the background component is enforced by the rank regularization and the spatial sparsity of the motion component is promoted by the sparsity regularization in framelets. The validation with both synthetic and experimental cardiac data and the comparison with the state-of-art reconstruction methods show that PRISM is feasible for maintaining the reconstruction quality with much fewer samples. The consequent reduction of data acquisition time can relax the breath-holding constraint with possibly less respiratory motion artifact and more regular heart rate in cardiac cine imaging, and enable the imaging of patients with faster heart rate in real-time cardiac cine imaging.**

***Index Terms*—Compressive sensing, matrix completion, robust PCA, low rank, sparsity, framelet, dynamic MRI, cardiac MRI.**

I. Introduction

DYNAMIC MRI reconstructs a temporal series of images to resolve the motion or the variation of the imaged object. It often occurs that the image frames to be reconstructed are dynamically correlated, which we term as "image coherence". As a result, the acquired MR data in *k-t* space are also dynamically coherent, which we name as "data redundancy". Over the years numerous spatiotemporal strategies have been proposed to accelerate dynamic MRI or improve reconstruction quality by exploring image coherence and/or data redundancy explicitly or implicitly. Some recent work includes UNFOLD [Madore99], *k-t* BLAST and *k-t* SENSE [Tsao03], HYPR [Mistretta06], *k-t* SPARSE [Lustig06], Partially Separable Functions (PSF) [Liang07], *k-t* FOCUSS [Jung09], *k-t* PCA [Pedersen09] and *k-t* SLR [Goud10].

Cardiac MRI, as perhaps the most challenging and inspiring dynamic MRI application, serves nowadays as a major imaging modality for noninvasive diagnosis of heart disease in clinic practice [Lee05, Finn06]. With fast scanning, such as the high-speed spiral sampling [Ahn86, Meyer92], which can be further enhanced by the parallel imaging [Sodickson97, Pruessmann99], cardiac MRI offers cine reconstruction of the beating heart through steady-state free precession (SSFP) cine imaging or real-time SSFP cine imaging.

A major need of cardiac MRI is the simultaneous realization of higher spatial and temporal resolution. However, they usually conflict each other [Lee05]. For example, in the ECG-gated cardiac cine imaging, both resolutions are limited by the tradeoff balance between them and the acquisition time, while the acquisition time is inherently limited by individual breath-holding time. On the other hand, despite without gating or breath-holding, the real-time cardiac cine imaging also suffers from the low resolution since the acquisition window is intrinsically restricted by the R-R interval.

In this paper, we are going to present a new model by further exploring the use of image coherence and data redundancy. Our approach addresses the question of maintaining the image quality with the least amount of the data. As a result, the total data acquisition time can be significantly reduced. In turn, the consequent relaxed requirement on the breath-holding time alleviates respiratory motion artifacts and regularizes the heart rate in cine imaging; the reduced data acquisition time allows the real-time cine imaging of the patients with fast heart rate.

That is, we introduce the "divide-and-conquer" spatiotemporal matrix decomposition approach, namely Prior Rank, Intensity and Sparsity Model (PRISM), for dynamic MRI with emphasis on cardiac MRI. PRISM is motivated by the abstracted observation that dynamically correlated images can usually be approximated by the superposition of the background component and the motion component. Here, the background component refers to temporally stationary or slowly varying component, and thus has a large degree of dynamic similarity or coherence; the motion component refers to dynamically moving or rapidly changing component, which is usually either sparse itself or can be sparsified in certain basis. The reason of this decomposition treatment is that each component can be mathematically regularized according to its own different characteristic. Thus we first "divide" the dynamic images into two matrix components in model, and "conquer" both components in reconstruction. Please notice that both components are assumed to be unknown and recovered simultaneously rather than to have been divided prior to the image reconstruction.

*H. Gao is with the Department of Mathematics, University of California, Los Angeles, CA 90095 USA (e-mail: haog@math.ucla.edu).

Y. Lin and O. Nalcioglu are with the John Tu and Thomas Yuen Center for Functional Onco-Imaging, University of California, Irvine, CA 92697 USA.

O. Nalcioglu is also with the Department of Cogno-Mechatronics Engineering, Pusan National University, Miryang 627-706, Republic of Korea.

C. B. Ahn is with the Department of Electrical Engineering, Kwangwoon University, Seoul 139-701, Republic of Korea.

Specifically, we enforce the temporal similarity or coherence of the background component through the rank regularization, and regularize the motion component through the sparsity regularization. Here both regularizations are with respect to the proper basis, i.e., in the transform domain rather than in the image domain. Moreover, other general prior facts or specific prior knowledge, such as the intensity characteristics of structures, can be based upon in PRISM. These ingredients are exactly the critical components and the name origin of PRISM.

This matrix decomposition idea was originally proposed and analyzed for the rank-sparsity incoherence [Chandrasekaran09] and the so-called Robust PCA (Principle Component Analysis) (RPCA) [Candes10]. In particular, the rank regularization in the context of matrix completion [Recht10, Candes09] can be regarded as sparser representation for matrices than the traditional sparsity for vectors [Donoho06, Candes06]. Inspired by RPCA, we have generalized it in the more appropriate form for image processing and medical imaging, with existing applications in computed tomography (CT). The first generalization, namely RPCA-4DCT model, included the sparsity regularization in the transform domain, such as total variation (TV) or tight framelet (TF) transform [Gao10]. Please notice that, due to its multilevel structure and redundant representation, the sparse regularization with TF is more efficient than that by TV or wavelet. The second generalization, i.e., PRISM, incorporated the rank regularization in the transform domain as well, besides the inclusion of intensity priors [Gao11].

Among the existing dynamic MRI techniques, several methods utilized the global property of the spatiotemporal matrix as a single entity, such as the use of PCA in *k-t* PCA [Pedersen09], the use of rank regularization based on PSF [Zhao10, Haldar10], the use of hybrid rank and sparsity regularization in *k-t* SLR [Goud11], and the presented results there showed that the global regularization for enforcing the image coherence considerably improves the reconstruction quality.

However, it is rarely the case that the dynamic images are low-rank. It should be more appropriate to model them as the supposition of the low-rank background component and the sparse motion component.

In the next section we will formulate the divide-and-conquer PRISM for dynamic MRI in the setting of cardiac MRI. Its validation will be presented with both synthetic and experimental data in the result section, where we will compare PRISM with the start-of-art techniques, such as sparsity regularization [Lustig07, Jung09], rank regularization [Zhao10, Haldar10], and hybrid rank and sparsity regularization [Goud11].

II. Methodology

A. Image Coherence and Data Redundancy

By image coherence, we mean the temporal similarity or coherence among image frames that often arise in dynamic MRI. By data redundancy, we mean the consequent data correlation or redundancy in k-space. By fully exploring the use of both image coherence and data redundancy, the scope of this article aims at maintaining the reconstruction quality with the least amount of data with emphasis on cardiac MRI. Consequently, the reduction of data acquisition time can relax the breath-holding constraint with less respiratory motion artifact and more regular heart rate in cardiac cine imaging, and enable the imaging of patients with faster heart rate in real-time cardiac cine imaging.

To utilize the image coherence, we will introduce the divide-and-conquer approach via PRISM. That is we view dynamic image frames as the supposition of the background component and the motion component, since each component can be mathematically regularized differently according to its own characteristic, i.e., the low-rank matrix regularization for the background component, and the sparse matrix regularization for the motion component, with row in space and column in frame. Despite the fact that cardiac image frames are rarely stationary or low-rank due to the motion, through PRISM, they are first "divided" into the coherent background component and the sparse motion component, and "conquered" through the appropriate mathematical regularization and solution algorithm. As a side remark, we can think of the low-rank matrix characterization as sparser transform than the frame-wise spatial sparse regularization, which intuitively allows to reconstruct with fewer data.

We briefly discuss the reduction of data redundancy for the potential speedup of dynamic MRI. First it is important to realize that the full dynamic dataset is redundant, which is the consequence of the image coherence between frames, i.e., the background component. In Sec. IIB, we will introduce a dynamic sampling strategy that, together with PRISM, is potentially capable of maintaining the image quality with much fewer samples. The key is to form the sampling pattern that is complementary between frames while being specific to each frame.

B. Dynamic Spiral Sampling

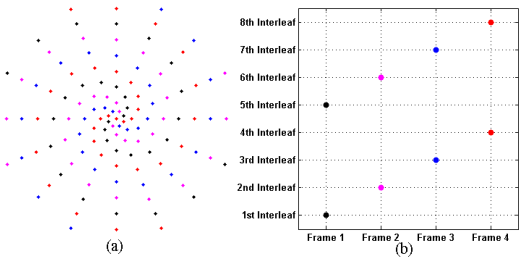

Fig. 1. Dynamic Spiral Sampling. The data samples for reconstructing an individual MRI image frame are acquired at the dynamically interleaved spiral interleaves in a periodic fashion. In this illustrative example, the dynamic spiral sampling pattern is repeated for every 4 MRI image frames, and the spiral interleaves belonging to each frame are colored differently. Therefore, 25% partial data are acquired, and the total data acquisition time can be reduced to ¼ or the temporal resolution can be increased by 4-fold.

To reduce the total data acquisition time, we adopt a dynamic sampling strategy as illustrated in Fig. 1. That is, instead of collecting all samples, we acquire samples partially

along those dynamically interleaved spiral interleaves in a periodic fashion. In any period, each interleaf is collected for one and only one frame so that there is no missing or overlapping of interleaves.

The immediate benefit of this dynamic sampling is the reduction of the total data acquisition time, which is proportional to the number of interleaves for each frame. Consequently, it promises us the access to cardiac cine imaging with higher temporal resolution or/and less breath-holding time, and real-time cardiac cine imaging with higher temporal or/and spatial resolution. For example, assuming 256 interleaves as the full dataset for each frame, 640 milliseconds as the usable R-R interval (TH), 4 milliseconds as the repetition time (TR), and 8 views per segment (VPS), the total acquisition time is about 20 seconds and the temporal resolution is 32 milliseconds with 20 frames. Using 8-fold downsampling, the possible gains include: the reduction of the total acquisition time to 2.5 seconds, which is almost breath-holding free; the 4 milliseconds temporal resolution with 160 frames; multi-slice imaging with 8 slices and 20 frames each. The above gains can be further increased through the parallel imaging and view-sharing technique.

However, without the proper reconstruction method, the MRI image quality can be severely degraded due to the downsampling. Before introducing our new reconstruction model PRISM and its solution algorithm, let us notice that the interleaves for individual frames in Fig.1 form complementary views so that any interleaf is covered for certain frame during each period. In this way, despite its downsampling, the proposed dynamic sampling strategy periodically fills up the missing common features for all frames, when in conjunction with PRISM.

C. *Forward Model: Regridding Method via Oversampling*

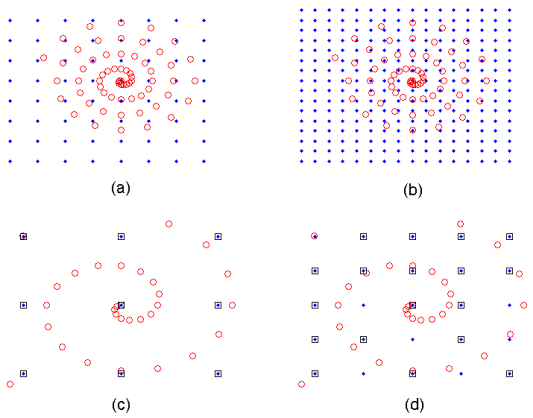

Fig. 2. Cartesian Oversampling. Here blue dots are on the Cartesian grid, red circles are on the spiral grid, and black squares are the corresponding nearest-neighbor Cartesian grid for the spiral grid. (a) The standard Cartesian grid; (b) the twice-oversampled Cartesian grid; (c) zoom-in view of the interpolation from the standard Cartesian grid to the spiral grid; (d) zoom-in view of the interpolation from the twice-oversampled Cartesian grid to the spiral grid.

To bridge from Cartesian grid to spiral grid in k-space, the appropriate interpolation, i.e., the regridding method, is required. Please note that we need the interpolation from Cartesian grid to spiral grid, not vice versa, since we will formulate the reconstruction problem as the model-based optimization problem in PRISM.

To maintain the accuracy of the regridding, we employ the oversampling strategy (Fig. 2). That is we first oversample the k-space (Fig. 2(b)), and then interpolate with the standard bilinear form (Fig. 2(d)). Due to its redundancy, this oversampling strategy reduces the interpolation error caused by the mismatch of grid density between spiral grid and Cartesian grid, particularly for the central low-frequency samples. Empirically the twice-oversampled Cartesian grid is generally sufficient for reconstruction. To avoid the inverse crime, the forward data are generated using much larger oversampling ratio. For example, 8-fold oversampling is utilized for a 2D 256×256 Cartesian grid, during which each spiral sample is usually interpolated from four unique Cartesian samples. In the future work, we will explore the possibility of more accurate regridding methods, such as the use of Pseudo-Polar Grid (PPG) together with Pseudo-Polar Fast Fourier Transform (PPFFT) that is mathematically exact from Cartesian grid to PPG [Averbuch06, Averbuch08, Lustig04], which is conceptually similar to the well-known linogram method in computed tomography [Buzug08].

Consequently, the forward model of spiral MRI can base upon this interpolation operator I and the discrete Fourier transform F, i.e., the matrix multiplication

$$M = I \cdot F \,, \tag{1}$$

which maps MRI images to the k-space spiral data.

Moreover, let P_j correspond to the dynamic selection of samples (Fig. 1) for the jth frame with N_t as the number of frames, i.e., a diagonally binary matrix with 1 (resp. 0) for the samples on (resp. off) the jth trajectory, and thus the system matrix of cardiac MRI can be formulated as

$$A = \{A_j = P_j \cdot M, \ j \le N_t\} \,, \tag{2}$$

which will be used next in PRISM as the forward model for cardiac MRI. To simplify the notation, we will use A for A_j for the rest of the paper without further remarks.

D. *PRISM*

The major contribution of this paper is to introduce the PRISM for dynamic MRI. As a spatiotemporal model, instead of individual reconstructing each frame, PRISM simultaneously reconstructs images at all frames using the "divide-and-conquer" approach. "Divide" means that all image frames as a single entity are modeled as the superposition of the background component and the motion component as explained in Sec. I and Sec. IIA; "conquer" means that each component is targeted with the pertinent mathematical regularization. Specifically, the dynamic coherence or similarity of the background component is enforced through the rank regularization up to certain transform; the sparsity of the motion component is promoted through the sparsity regularization up to the proper basis. Please notice that both mathematical regularizations are consistent with the empirical

fact that, image frames usually share the similar background, while each frame has its unique feature that are approximately sparse in certain basis. This motivated the PRSIM [Gao11], which generalizes the model in [Gao10].

Because of the fusion of all frames through PRISM, dynamic images to be reconstructed are a single matrix rather than multiple vectors. That is

$$X = \lfloor x_1 \quad \cdots \quad x_j \quad \cdots \quad x_{N_t} \rfloor, \tag{3}$$

where X is the matrix representing dynamic images with N_t temporal frames, and x_j is the column vector corresponding to the sorted spatial pixels in the jth frame.

Following the "divide-and-conquer" approach, as an alternative for directly reconstructing X, we introduce a pair of unknown matrices: X_L denotes the low-rank background component and X_S denotes the sparse motion component.

$$X = X_L + X_S . \tag{4}$$

As mentioned in Sec. I and Sec. IIA, this decomposition (4) offers an alternative view of dynamic images that is consistent with the practice. More importantly, it is mathematically pertinent since each component can be regularized accordingly with its unique feature, i.e., the temporal rank of the background and the spatial sparsity of the motion. Besides, it is sometimes desirable to separate the motion from the background, which is exactly the outcome of (4). Moreover, we can obtain both components with roughly the same computational cost for X, using the split Bregman method in Sec. IIE.

The goal of PRISM is to recover both X_L and X_S. And X can be obtained as a consequence of (4). The "conquer" step in PRISM is through the following regularization,

$$R(X) = \lambda_* \| T_L(X_L) \|_* + \lambda_1 \| T_S(X_S) \|_1 + \lambda_t \| X \|, \tag{5}$$

where T_L (resp. T_S) denotes some proper transform so that the component is more low-rank (resp. sparser), $\|\cdot\|_*$ the nuclear norm for penalizing the matrix rank, which is defined as the sum of its singular values $\{\sigma_k\}$ with the regularizing parameter λ_*, i.e.,

$$\| X \|_* = \sum_k \sigma_k , \tag{6a}$$

$\|\cdot\|_1$ the L_1 norm for promoting the sparsity, which is defined as the absolute sum of its entries or the sum of the L_1 norm of each column vector (image frame) with the regularizing parameter λ_1, i.e.,

$$\| X \|_1 = \sum_j \| x_j \|_1 , \tag{6b}$$

and $\|\cdot\|$ is certain regularizing norm on the total images with the regularizing parameter λ_t.

In this study, we select T_L to be the identity transform and T_S to be the tight framelet transform (TF) [Ron97, Daubechies03, Dong10] denoted by W, and the regularization norm on total images X to be W as well. That is,

$$R(X) = \lambda_* (\| X_L \|_* + r \| WX_S \|_1) + \lambda_t \| WX \|_1 , \tag{7}$$

and the choice of parameters will be clarified in Sec. IIE. TF can be regarded as a generalization of total variation transform [Rudin92] and wavelet transform [Daubechies92]. Due to its multiscale structure and redundant representation, TF is extremely rich in terms of the dictionary for sparse representation. In this study, a multilevel tight framelet decomposition without downsampling under the Neumann (symmetric) boundary condition is used with piecewise linear framelets [Chai07, Cai08].

Combining the forward model (2) of cardiac MRI and the regularization term (7) for modeling background coherence and motion sparsity, PRISM is formulated as the following optimization problem for solving X_L and X_S

$$(X_L, X_S) = \arg\min_{(X_L, X_S)} \frac{1}{2} \| AX - Y \|_2^2 + R(X) . \tag{8}$$

Please notice that PRISM can be further strengthened when the intensity-based prior information on X is available [Gao11].

E. Solution Algorithm via Split Bregman Method

In this section, we develop an efficient solution algorithm to the model problem (8) involving the non-differentiable L_1-type norms. The algorithm is based on split Bregman method [Osher05]. That is we optimize (8) with the regularization term replaced by its Bregman distance, and consequently (8) is simplified to the "add-noise-back" iterative scheme. The similar strategy can be utilized for relaxing the non-differentiable L_1 norms by introducing some dummy variables [Goldstein09]. We summarize the solution algorithm based on split Bregman method in Fig. 3 without deriving it and refer the interested readers to [Osher05, Goldstein09, Cai09] for theory and other details.

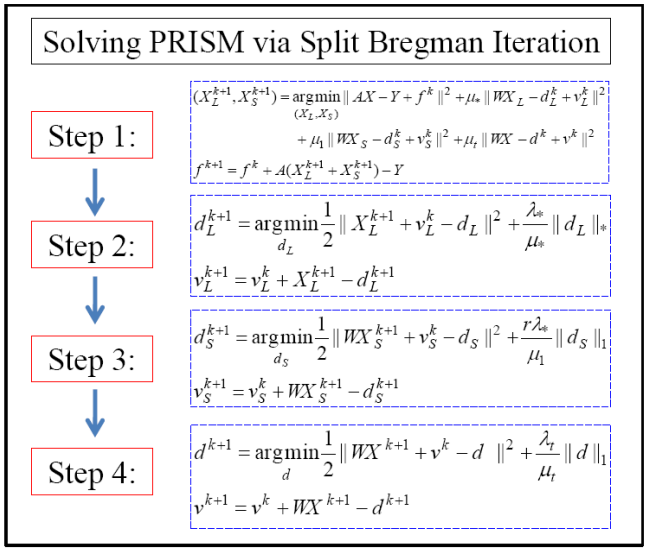

Fig. 3. Solution Algorithm by Split Bregman Method. The algorithm is composed of a single loop with four steps, initialized with zeros, i.e., $X_L^0 = X_S^0 = 0$, $f^0 = 0$, $d_L^0 = v_L^0 = 0$, $d_S^0 = v_S^0 = 0$ and $d^0 = v^0 = 0$. Here, d_L, d_S, and d are dummy variables for relaxing the non-differentiable nuclear norm of X_L, TF norm of X_S, and TF norm of X respectively; f and v's come from optimizing the Bregman distance of regularization terms, and are updated with the add-residual-back formula. Step 1: the update of X_L and X_S by the standard L_2 minimization. Step 2: the update of d_L by SVT formula (9). Step 3: the update of d_S by the shrinkage formula (11a). Step 4: the update of d by the shrinkage formula (11b).

As shown in Fig. 3, the model problem (8) is solved through a single split Bregman loop involving four steps. The first step

corresponds to one iteration step in a standard L_2 minimization, and the solution is simply from its optimal condition. The resulting linear system can be solved through conjugate gradient method (CG), during which the explicit matrix inversion is avoided by matrix multiplications and additions, such as AX and WX.

The second step has the explicit formula, i.e., the so-called singular value thresholding (SVT) [Cai10],

$$d_L^{k+1} = D_{\lambda_*/\mu_*}(X_L^{k+1} + v_L^k), \tag{9}$$

where the thresholding is with respect to singular values σ of the input matrix, i.e.,

$$\begin{aligned} X &= U \cdot \mathrm{diag}(\sigma) \cdot V^T \\ D_\tau(X) &= U \cdot \mathrm{diag}(\max(\sigma - \tau, 0)) \cdot V^T \end{aligned}. \tag{10}$$

The major computational cost of (10) is from singular value decomposition (SVD). However overall it is computationally negligible, since the number of columns of the matrix considered here or image frames is considerably small. If necessary, the fast computation of SVT can be utilized, such as the one without SVD [Cai10].

Similarly, the third and the fourth step have the analytical solution as well, i.e., the so-called shrinkage formula,

$$d_S^{k+1} = T_{r\lambda_*/\mu_1}(WX_S^{k+1} + v_S^k), \tag{11a}$$

$$d^{k+1} = T_{\lambda_t/\mu_t}(WX^{k+1} + v^k), \tag{11b}$$

with the shrinkage operator defined as

$$T_\tau(X) := \mathrm{sgn}(X) \cdot \max(|X| - \tau, 0). \tag{12}$$

Please note that the shrinkage formula (11) is a local scalar operation for each entry, while SVT (9) is a global matrix operation.

For the regularization parameters in Fig. 3, we recommend

$$r = \max(n_1, n_2)^{-1/2} \text{ and } \mu_t = \mu_* = \mu_1 = \lambda_t = \lambda_*, \tag{13}$$

with n_1 (n_2) as the number of rows (columns) of the matrix X. Here the choice of r is supported by the rigorous analysis for RPCA [Candes10]. Empirically, $\lambda_* \in [0.1, 10]$ is sufficient in terms of both accuracy and speed.

Overall, the computationally dominant component of Fig. 3 is the first step for updating X_L and X_S. In this step solved by CG, it is not necessary to solve it with very high accuracy in order for the main loop to achieve fast convergence, besides the fact that the resulting linear system from the optimal condition has a relatively small condition number for dynamic MRI (2). We find that CG with 10 inner iterations is adequate for the algorithm to have the acceptable reconstruction accuracy within 30 split Bregman iterations.

F. Summary of Reconstruction Methods for Comparison

In the result section, we compared the divide-and-conquer PRISM (8) with the classic model "FFT" with X regularized by L_2 norm when the system is underdetermined, i.e.,

$$R(X) = \lambda_2 \| X \|_2^2, \tag{14}$$

and other three state-of-art approaches: the model "TF" with X regularized by TF norm that is similar to *k-t* SPARSE [Lustig07] and *k-t* FOCUSS [Jung09]

$$R(X) = \lambda_1 \| WX \|_1, \tag{15}$$

the model "LR" with X regularized by nuclear norm that is similar to MC-based PSF [Zhao10, Mallad10]

$$R(X) = \lambda_* \| X \|_*, \tag{16}$$

and the model "TF-LR" with X regularized by the hybrid TF and nuclear norm that is similar to *k-t* SLR [Goud11]

$$R(X) = \lambda_* \| X \|_* + \lambda_1 \| WX \|_1. \tag{17}$$

G. Comparison Setting with Synthetic Data

We compared reconstruction results from PRISM and other methods with the synthetic cardiac phantom (Fig. 4) as the ground truth. To avoid the inverse crime, the spiral data were generated with 8-fold oversampling (Fig. 2). In reconstruction, the forward model (2) with the twice-oversampled regridding method was utilized for all reconstructions.

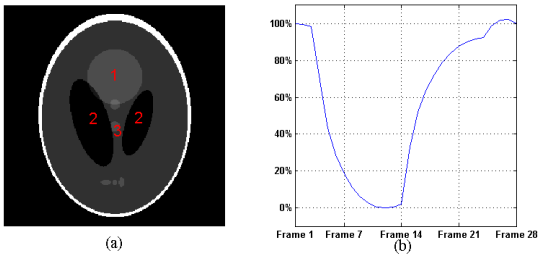

(a) (b)

Fig. 4. Components of Synthetic Cardiac Phantom: (a) the modified Shepp-Logan phantom; (b) the cardiac phases according to the established model [Wang02]. The temporal variations consist of the intensity increase and the area change of the top circle "1" to model the heart motion, the horizontal movement of two ellipses "2" to model the lung motion, and the vertical movement of the lower central circle "3" to model the small deformation.

The synthetic cardiac phantom with 28 temporal frames was constructed based upon the 256×256 Shepp-Logan phantom (Fig. 4a) with the dynamic change following the established cardiac motion model [Wang02] (Fig. 4b).

The spiral data were acquired through dynamic sampling (Fig. 1) with each period involving 8 frames and 32 interleaves for each frame, i.e., 12.5% partial data. This 8-fold reduction of k-space spiral interleaves corresponds to the reduction of data acquisition time to 1/8 or the increase of temporal resolution by 8-fold. The same 1% Gaussian noise was added to the data for all reconstructions.

H. Comparison Setting with Experimental Data

With the experimental cardiac data, the reconstruction images from "FFT" using the full dataset were regarded as the ground truth (Fig. 6). Again, the forward model (2) with the twice-oversampled regridding method was utilized.

The experimental data were measured for a volunteer at 1.5 Tesla whole body MRI (CHORUS, ISOL Co). Balanced spiral SSFP sequence was used for cardiac cine imaging with a breath hold. The repetition time was 4miliseconds with echo time of 1miliseconds. The number of interleaves was 256, and the number of interleaves per segment was 8. Total 28 frames were measured. Flip angle was 15 degrees, slice thickness was 8mm, and field-of-view (FOV) was 400mm.

Ideally, the cardiac data can be acquired directly through dynamic sampling (Fig. 1) by modifying the MRI pulse sequence accordingly. However, in this proof-of-concept study, the full dataset was acquired instead, and then post-selected according to the aforementioned dynamic sampling (Fig. 1) to form the 25% partial data and 12.5% partial data respectively.

All the reconstruction results had 28 temporal frames with 256×256 spatial resolution. Please notice that the quantitative comparison was biased towards "FFT" since the images from "FFT" with the full dataset were referred as the ground truth.

III. Results

A. Synthetic Cardiac Data

With the simulation setup in Sec. IIG, the reconstructed images from various models in Sec. IIF with 12.5% partial data are presented in Fig. 5.

As shown in Fig. 5, comparing with the synthetic cardiac phantom (Fig. 4), the reconstructed image quality was severely degraded by the classic approach "FFT", with spiral artifacts, blurring and missing of small features, such as those small ellipses at the bottom (Fig. 4(a)); the state-of-art methods "TF", "LR", and "TF-LR" improved the image quality, however some details were still missing and a few spiral artifacts survived; in contrast, PRISM reconstructed not only those missing features, but also the overall images with the least error. This is also consistent with the quantitative comparison with the ground truth as summarized in Table I. In summary, it is clear that PRISM offered the best image quality due to its divide-and-conquer decomposition approach with rank regularization on the background component and sparsity regularization on the motion component.

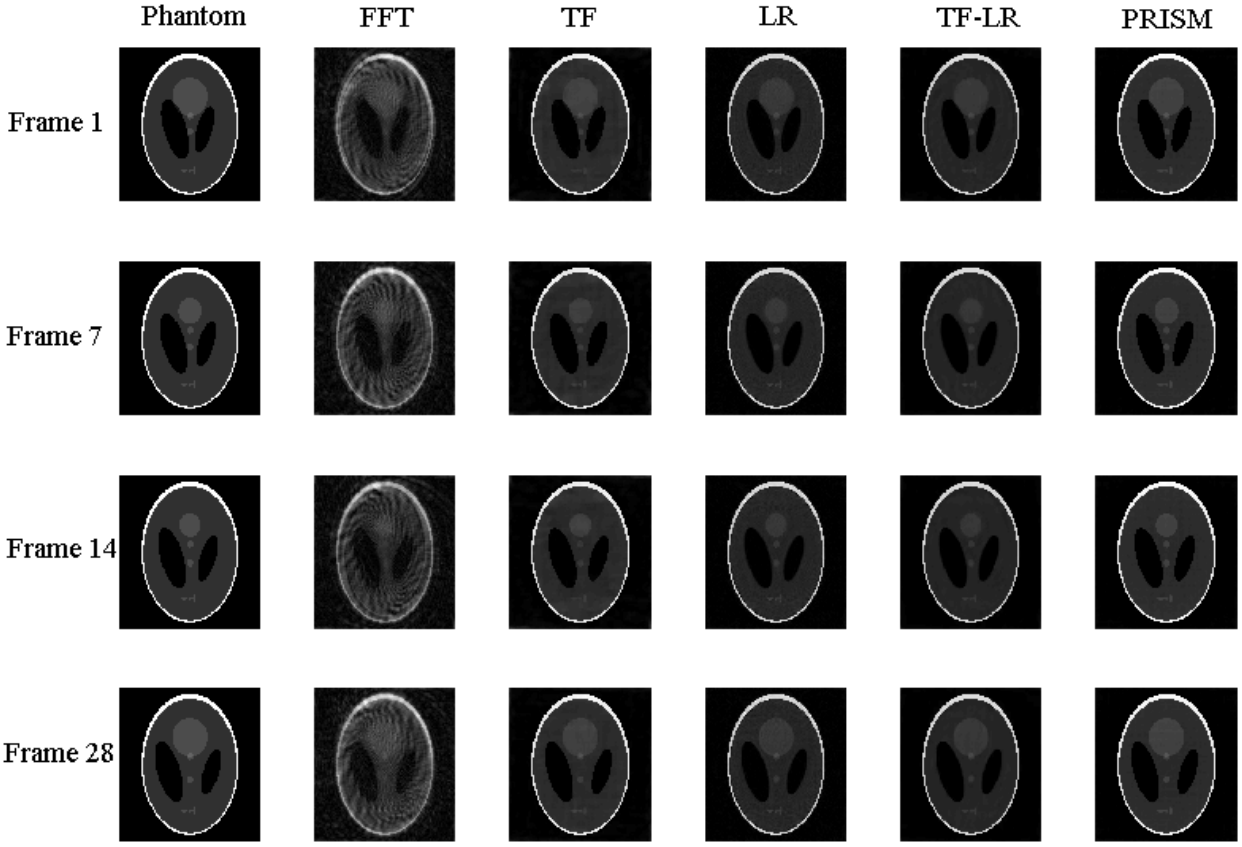

Fig. 5. Reconstructions with 12.5% Synthetic Data. The ground truth in the 1st column was based upon on the synthetic cardiac phantom (Fig. 4). With 12.5% partial dataset from dynamic sampling (Fig. 1), reconstructed images with FFT, TF, LR, TF-LR, PRISM are displayed in the 2nd to 6th columns respectively.

B. Experimental Cardiac Data

With the simulation setup in Sec. IIH, the reconstructed images from various models in Sec. IIF with 25% partial data and 12.5% partial data are presented in Fig. 6 and Fig. 7 respectively. Here the reconstructed images from "FFT" with the full dataset were used as the ground truth for comparison. Please note that the zoom-in views of the heart are displayed in Fig. 6 and 7 for clarity.

As shown in Fig. 6 and Fig. 7, PRISM still offered the best reconstruction image quality among all methods when using the experimental cardiac data. Similar to the comparison with synthetic data, "FFT" blurred the images with severe spiral artifacts; despite the improved image quality, the state-of-art techniques "TF", "LR", "TF-LR" still missed some details; in contrast, the reconstructed images from PRISM were quite satisfactory in terms of overall image quality and small feature recovery. The quantitative error is also summarized in Table I.

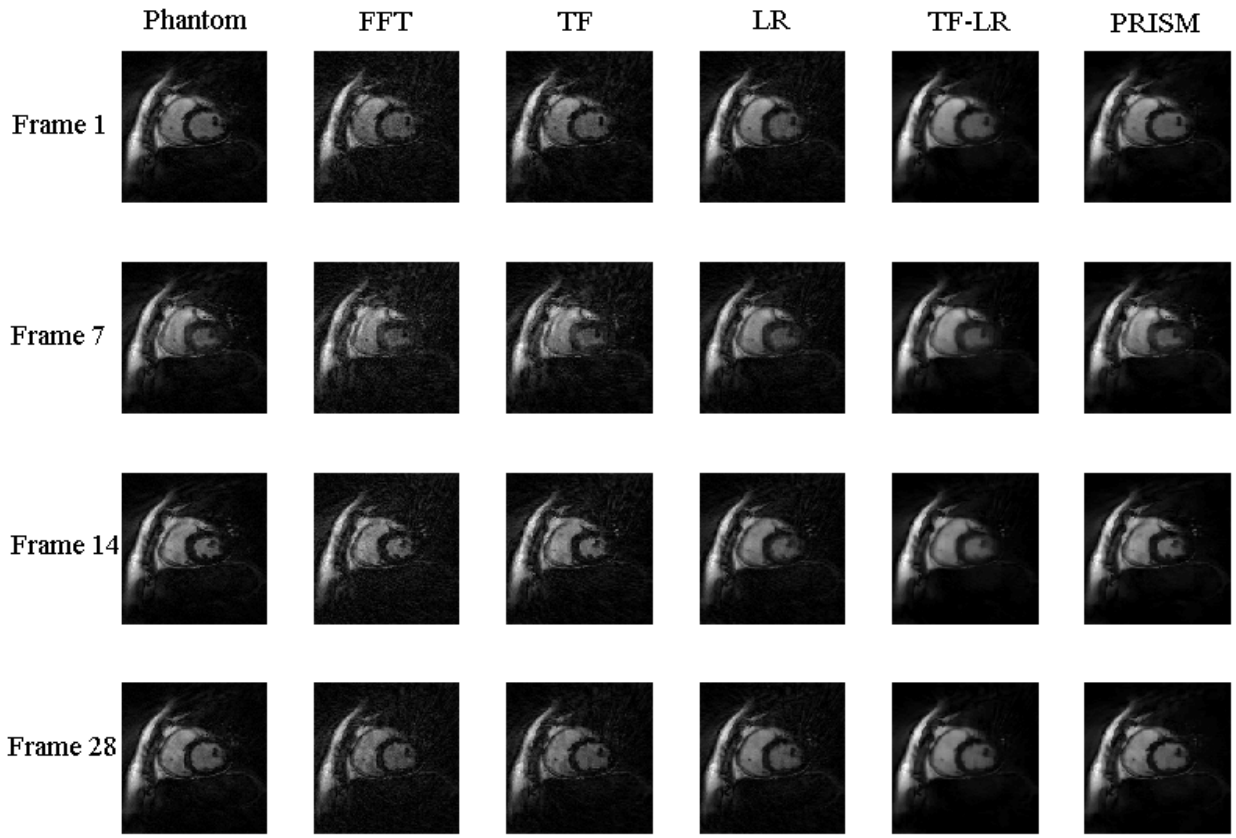

Fig. 6. Reconstructions with 25% Cardiac MRI Data. The ground truth in the 1st column was obtained with FFT using the full dataset. With 25% partial dataset from dynamic sampling (Fig. 1), reconstructed images with FFT, TF, LR, TF-LR, PRISM are displayed in the 2nd to 6th columns respectively.

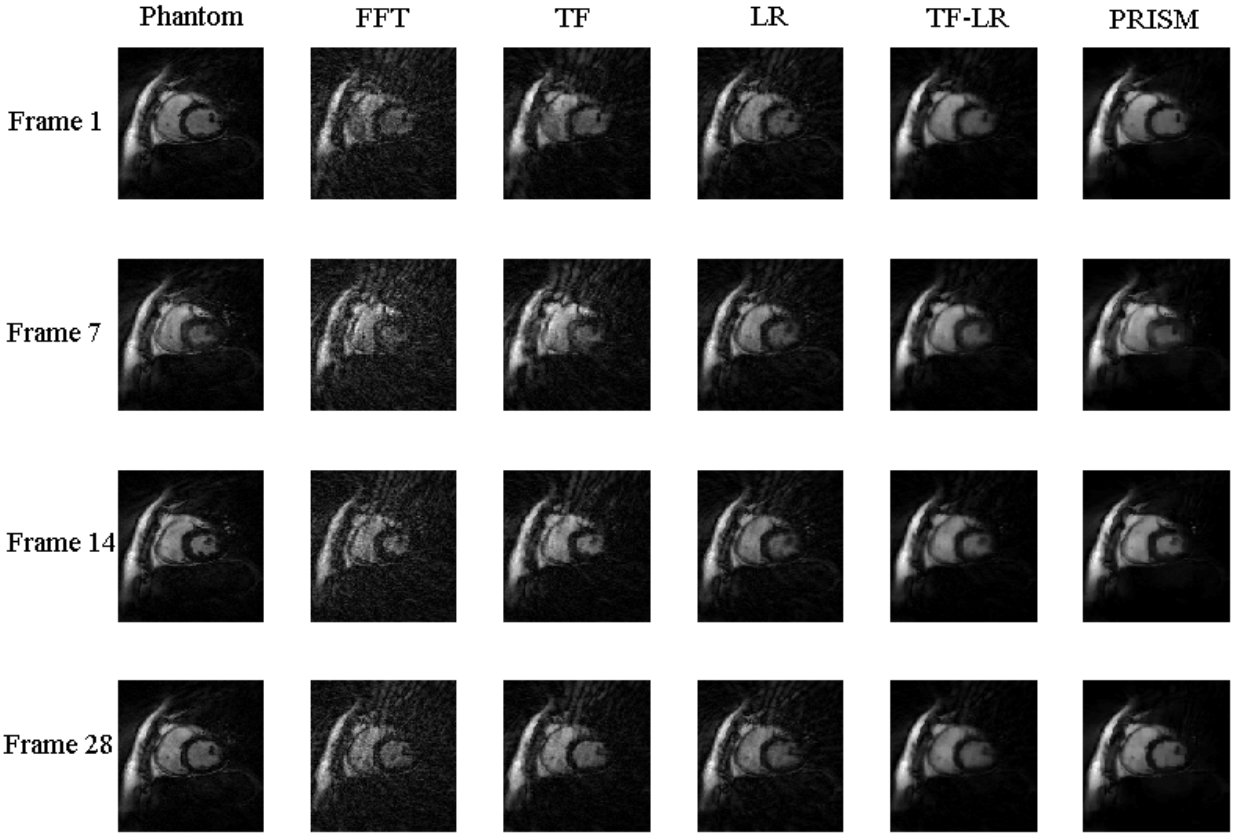

Fig. 7. Reconstructions with 12.5% Cardiac MRI Data. The ground truth in the 1st column was obtained with FFT using the full dataset. With 12.5% partial dataset from dynamic sampling (Fig. 1), reconstructed images with FFT, TF, LR, TF-LR, PRISM are displayed in the 2nd to 6th columns respectively.

III. Conclusion

We have introduced the divide-and-conquer matrix decomposition model, namely PRISM, for dynamic MRI with emphasis on cardiac MRI. Through model comparison with both synthetic and experimental data, we have validated that PRISM is superior to some state-of-art approaches, and has the potential for maintaining the reconstruction image quality with much fewer samples. Here the total data acquisition time of experimental cardiac data took roughly 24 seconds. With 12.5% partial data, the reconstruction result from PRISM was quite satisfactory (Fig. 7). If only those 12.5% partial data were acquired experimentally, this would correspond to the reduction of total data acquisition time to 3 seconds, which is almost free of the breath hold.

In this proof-of-concept study, the dynamic sampling was realized through the post-selection of the acquired full spiral dataset. In the future work, the real-time dynamic sampling will be investigated.

The regridding method as part of the forward model is crucial for the image quality, since Cartesian grid and spiral grid have the different sampling density distribution, particularly for those low-frequency samples near the origin. In the future work, we will further study the regridding method, e.g., the one based on PPG together with PPFFT.

Last but not the least, PRISM should be more robust and accurate when incorporating the image registration into the model. This would reflect more temporal coherence than the current version since the registered images share more similarity. As a result, the MRI data can be more redundant with respect to the reconstruction to allow for further reduction of data acquisition time, or higher temporal or spatial resolution in dynamic MRI, particularly cardiac MRI.

TABLE I

RECONSTRUCTION ACCURACY WITH VARIOUS MODELS. THE METRICS IS DEFINED AS $\|X- X^0\|/\| X^0\|$ WITH $\|\cdot\|$ AS THE L_2 NORM. HERE, X^0 FOR SYNTHETIC DATA IS THE CARDIAC PHANTOM (FIG. 4); X^0 FOR EXPERIMENTAL DATA IS RECONSTRUCTED FROM "FFT" WITH THE FULL DATASET.

	FFT	TF	LR	TF-LR	PRISM
12.5% SYNTHETIC DATA	0.328	0.072	0.085	0.063	0.025
25% CARDIAC DATA	0.183	0.103	0.096	0.104	0.052
12.5% CARDIAC DATA	0.256	0.157	0.138	0.115	0.077

Acknowledgment

The authors thank Dr. Stanley Osher with UCLA for valuable discussions and inputs on dynamic MRI, and Dr. Ge Wang with Virginia Tech. for helpful discussions on the cardiac model and cardiac MRI. This work was supported in part by the World Class University Program through the National Research Foundation of Korea funded by the Ministry of Education, Science and Technology, Republic of Korea (grant no. R31-20004-(ON)).

References

[1] B. Madore, G. Glover, and N. Pelc, "Unaliasing by fourier-encoding the overlaps using the temporal dimension (UNFOLD), applied to cardiac imaging and fMRI", *Magn. Reson. Med.*, 42, 813-828 (1999).

[2] J. Tsao, P. Boesiger, and K. P. Pruessmann, "*k-t* BLAST and *k-t* SENSE: Dynamic MRI with high frame rate exploiting spatiotemporal correlations", *Magn. Reson. Med.*, 50, 1031-1042 (2003).

[3] C. A. Mistretta, O. Wieben, J. Velikina, W. Block, J. Perry, Y. Wu, K. Johnson, and Y. Wu, "Highly constrained backprojection for time-resolved MRI", *Magn. Reson. Med.*, 55, 30-40 (2006).

[4] M. Lustig, J. M. Santos, D. L. Donoho, J. M. Pauly, "*k-t* SPARSE: High frame rate dynamic MRI exploiting spatio-temporal sparsity", In Proceedings of the 13th Annual Meeting of ISMRM, 2420 (2006).

[5] Z.-P. Liang, "Spatiotemporal imaging with partially separable functions," Proc. 2007 IEEE Intl. Sym. Biomed. Imag., 988-991 (2007).

[6] H. Jung, J. Park, J. Yoo, and J. C. Ye, "Radial *k-t* FOCUSS for high-resolution cardiac cine MRI", *Magn. Reson. Med.*, 61, 103-116 (2009).

[7] H. Pedersen, S. Kozerke, S. Ringgaard, K. Nehrke, and W. Y. Kim, "*k-t* PCA: temporally constrained *k-t* BLAST reconstruction using principal component analysis", *Magn. Reson. Med.*, 62, 706-716 (2009).

[8] S. Goud, Y. Hu, and M. Jacob, "Real-time cardiac MRI using low-rank and sparsity penalties", in Proceedings of the ISBI (2010).

[9] V. S. Lee, *Cardiovascular MRI: physical principles to practical protocols.* Philadelphia: Lippincott Williams & Wilkins (2005).

[10] J. P. Finn, K. Nael, V. Deshpande, O. Ratib, and G. Laub, "Cardiac MR imaging: state of the technology", *Radiology*, 241, 338-354 (2006).

[11] C. B. Ahn, J. H. Kim, and Z. H. Cho, "High-speed spiral-scan echo planar NMR imaging – I", *IEEE Trans. Med. Imaging*, MI-5, 2-7 (1986).

[12] C. H. Meyer, B. S. Hu, D. G. Nishimura, and A. Macovski, "Fast spiral coronary artery imaging", *Magn. Reson. Med.*, 28, 202-213 (1992).

[13] D. K. Sodickson, and W. J. Manning, "Simultaneous acquisition of spatial harmonics (SMASH): fast imaging with radiofrequency coil arrays", *Magn. Reson. Med.*, 38, 591-603 (1997).

[14] K. P. Pruessmann, M. Weiger, M. B. Scheidegger, and P. Boesiger, "SENSE: sensitivity encoding for fast MRI", *Magn. Reson. Med.*, 42, 952-962 (1999).

[15] V. Chandrasekaran, S. Sanghavi, P. Parrilo, and A. Willsky, "Rank-sparsity incoherence for matrix decomposition", Preprint. (2009).

[16] E. J. Candès, X. Li, Y. Ma, and J. Wright, "Robust principal component analysis?", Technical report, Stanford University (2009).

[17] B. Recht, M. Fazel, and P. Parrilo, "Guaranteed Minimum-Rank Solutions of Linear Matrix Equations via Nuclear Norm Minimization", *SIAM Review*, 52, 471-501 (2010).

[18] E. J. Candès, and B. Recht, "Exact matrix completion via convex optimization," *Foundations of Computational Mathematics*, 9, 717-772 (2009).

[19] D. L. Donoho, "Compressed sensing", *IEEE Trans. Inf. Theory*, 52, 1289-306 (2006).

[20] E. J. Candès, J. Romberg, and T. Tao, "Robust uncertainty principles: exact signal reconstruction from highly incomplete frequency information", *IEEE Trans. Inf. Theory*, 52, 489-509 (2006).

[21] H. Gao, J. F. Cai, Z. Shen, and H. Zhao, "Robust principle component analysis based four-dimensional computed tomography". *UCLA CAM Report,* 10-79 (2010).

[22] H. Gao, J. F. Cai, Z. Shen, and H. Zhao, "Robust principle component analysis based four-dimensional computed tomography". *Phys. Med. Biol.*, In Press (2011).

[23] H. Gao, H. Yu, and G. Wang, "True-color CT based on a Prior Rank, Intensity and Sparsity Model (PRISM)". *UCLA CAM Report*, 11-01 (2011).

[24] B. Zhao, J. P. Haldar, C. Brinegar, and Z.-P. Liang, "Low rank matrix recovery for real-time cardiac MRI", in Proceedings of the ISBI (2010).

[25] J. Haldar, and Z.-P. Liang, "Spatiotemporal imaging with partially separable functions: a matrix recovery approach", in Proceedings of the ISBI (2010).

[26] S. Goud, Y. Hu, E. DiBella, and M. Jacob, "Accelerated dynamic MRI exploiting sparsity and low-rank structure: k-t SLR", *IEEE Trans. Med. Imaging*, In Press (2011).

[27] M. Lustig, D. L. Donoho, and J. M. Pauly, "Sparse MRI: the application of compressed sensing for rapid MR imaging", *Magn. Reson. Med.*, 58, 1182-1195 (2007).
[28] A. Averbuch, R. Coifman, D. Donoho, M. Elad, and M. Israeli, "Fast and accurate polar Fourier transform", *Appl. Comput. Harmon. Anal*., 21, 145-167 (2006).
[29] A. Averbuch, R. Coifman, D. Donoho, M. Israeli, and Y. Shkolnisky, "A framework for discrete integral transformations I — the pseudopolar fourier transform", *SIAM J. Sci. Comput*., 30, 785-803 (2008).
[30] M. Lustig, J. Tsaig,J. H. Lee, and D. Donoho, "Fast spiral fourier transform for iterative MR image reconstruction", IEEE International Symposium on Volume 1, 15-18 (2004).
[31] T. Buzug, *Computed Tomography: From Photon Statistics to Modern Cone-Beam CT*, Springer-Verlag (2008).
[32] A. Ron and Z. Shen, "Affine systems in $L_2(R^d)$: the analysis of the analysis operator", *J. Funct. Anal.*, 148, 408-447 (1997).
[33] I. Daubechies, B. Han, A. Ron, and Z. Shen, "Framelets: MRA-based constructions of wavelet frames", *Applied and Computational Harmonic Analysis*, 14, 1-46 (2003).
[34] B. Dong and Z. Shen, "MRA based wavelet frames and applications", IAS Lecture Notes Series, Summer Program on "The Mathematics of Image Processing", Park City Mathematics Institute (2010).
[35] L. Rudin, S. Osher, and E. Fatemi, "Nonlinear total variation based noise removal algorithms", *J. Phys. D*, 60, 259-268 (1992).
[36] I. Daubechies, *Ten lectures on wavelets*, vol. 61 of CBMS-NSF Lecture Notes, SIAM (1992).
[37] A. Chai and Z. Shen, "Deconvolution: a wavelet frame approach", *Numer. Math.*, 106, 529-587 (2007).
[38] J. F. Cai, R. H. Chan, and Z. Shen, "A framelet-based image inpainting algorithm", *Appl. Comput. Harmon. Anal.*, 24, 131-149 (2008).
[39] S. Osher, M. Burger, D. Goldfarb, J. Xu, and W. Yin, "An iterative regularization method for total variation-based image restoration", *Multiscale Model. Simul.*, 4, 460-489 (2005).
[40] T. Goldstein and S. Osher, "The split Bregman algorithm for l1 regularized problems", *SIAM J. Imaging Sci.*, 2, 323-343 (2009).
[41] J. F. Cai, S. Osher, and Z. Shen, "Split Bregman methods and frame based image restoration", *Multiscale Model. Simul.*, 8, 337-369 (2009).
[42] J. F. Cai, E.J. Candès, and Z. Shen, "A singular value thresholding algorithm for matrix completion", *SIAM J. Optimiz.*, 20, 1956-1982 (2010).
[43] J. F. Cai and S. Osher, "Fast singular value thresholding without singular value decomposition", *UCLA CAM Report*, 10-24 (2010).
[44] G. Wang, S. Zhao and D. Heuscher, "A knowledge based cone beam X-ray CT algorithm for dynamic volumetric cardiac imaging", *Med. Phys.*, 29, 1807-1822 (2002).